Rutile-type Ge$_x$Sn$_{1-x}$O$_2$ alloy layers lattice-matched to TiO$_2$ substrates for device applications

Hitoshi Takane[1*] , Takayoshi Oshima[2*] , Takayuki Harada[3] , Kentaro Kaneko[4] , and Katsuhisa Tanaka[1]

[1]Department of Material Chemistry, Kyoto University, Kyoto 615-8510, Japan
[2]Research Center for Electronic and Optical Materials, National Institute for Materials Science, Tsukuba, Ibaraki 305-0044, Japan
[3]Research Center for Materials Nanoarchitectonics, National Institute for Materials Science, Tsukuba, Ibaraki 305-0044, Japan
[4]Research Organization of Science and Technology, Ritsumeikan University, Kusatsu, Shiga 525-8577, Japan

*E-mail: takane.hitoshi.33v@st.kyoto-u.ac.jp; OSHIMA.Takayoshi@nims.go.jp

We report the characterization and application of mist-CVD-grown rutile-structured Ge$_x$Sn$_{1-x}$O$_2$ ($x = \sim$0.53) films lattice-matched to isostructural TiO$_2$(001) substrates. The grown surface was flat throughout the growth owing to the lattice-matching epitaxy. Additionally, the film was single-crystalline without misoriented domains and TEM-detectable threading dislocations due to the coherent heterointerface. Using the Ge$_{0.49}$Sn$_{0.51}$O$_2$ film with a carrier density of 7.8×10^{18} cm^{-3} and a mobility of 24 cm^{2}V^{-1}s^{-1}, lateral Schottky barrier diodes were fabricated with Pt anodes and Ti/Au cathodes. The diodes exhibited rectifying properties with a rectification ratio of 8.2×10^4 at ±5 V, showing the potential of Ge$_x$Sn$_{1-x}$O$_2$ as a practical semiconductor. © 2024 The Author(s). Published on behalf of The Japan Society of Applied Physics by IOP Publishing Ltd

Rutile-type (r-) metal oxides, such as r-GeO$_2$, r-SnO$_2$, r-TiO$_2$, and their alloys, have recently emerged as a new class of wide-band-gap semiconductors, due to their favorable electrical properties.[1,2] Very recently, r-GeO$_2$ has attracted attention as a novel semiconductor having superior physical properties, including the widest direct bandgap (E_g) of 4.68 eV,[3] theoretically-predicted ambipolar dopability,[4,5] estimated electron/hole mobilities as high as 244–377/27–29 cm^2 V^{-1} s^{-1},[6,7] and n-/p-type Baliga figure of merits of 270–350/27–30 $\times 10^8$ V^2 Ω^{-1} cm^{-2} surpassing those of SiC and GaN.[1] However, the epitaxial growth of r-GeO$_2$ remains challenging due to the severe volatility of GeO$_x$ at high temperatures,[1,8–10] hindering its device applications to date. On the other hand, r-SnO$_2$ and r-TiO$_2$ have also become important components within the rutile oxide framework, though they have been well-known conventional n-type oxide semiconductors and often applied for transparent conductive films[11,12] and thin-film transistors[13,14] so far. r-SnO$_2$ has the second widest E_g of 3.6 eV[15] among the rutile-type oxide semiconductors and has recently been regarded as an end member of the r-Ge$_x$Sn$_{1-x}$O$_2$ alloy.[2] Also, r-TiO$_2$ with a narrower E_g of 3.0 eV[16] is usually used as a substrate for rutile-type oxide films because of the availability of bulk single crystal. Bulk single crystals of r-GeO$_2$ and r-SnO$_2$ can be also synthesized by flux and vapor transport methods,[5,17–21] but substrates with sufficient area and quality for systematic epitaxy experiments have not been prepared yet. Previously, successful growth of r-Ge$_x$Sn$_{1-x}$O$_2$ alloy on r-TiO$_2$ has been reported, as some research groups including ours have achieved epitaxial stabilization of single-crystalline r-Ge$_x$Sn$_{1-x}$O$_2$ alloy films up to $x = 0.96$ on r-TiO$_2$ substrates, enabling us to control the E_g within the range of 3.8 and 4.4 eV.[2,22,23]

For device applications of r-Ge$_x$Sn$_{1-x}$O$_2$ alloy films, improving the crystalline quality of the films is necessary. Though it is feasible to grow the alloy films, a significant number of dislocations were observed in the films with $x = 0$ and 0.96, because of the large lattice mismatches with the TiO$_2$ substrate.[2,24–26] These dislocations degrade the electrical properties of the films as they act as scattering/trap centers and leakage paths, leading to an increase in on-resistance and premature breakdown. Therefore, the dislocation density must be minimized for potential power-device applications. One solution to this issue is epitaxial lateral overgrowth (ELO), which is a proven method in the field of GaN heteroepitaxy.[27,28] In our previous study, we conducted selective-area growth of r-SnO$_2$ on a SiO$_2$-masked r-TiO$_2$ substrate and verified the creation of dislocation-free areas in the lateral overgrown regions.[29] These findings indicate the potential to produce alloy films with reduced dislocation densities through ELO. However, achieving ELO films with high in-plane uniformity would require significant effort. The other solution is lattice-matching epitaxy, which is a fundamental strategy in the heteroepitaxial growth of semiconductor alloy systems.[30,31] The lattice constants of r-TiO$_2$ ($a = 4.594$ Å, $c = 2.959$ Å)[32] fall between those of r-GeO$_2$ ($a = 4.398$ Å, $c = 2.863$ Å)[32] and r-SnO$_2$ ($a = 4.738$ Å, $c = 3.187$ Å),[32] making this method applicable for r-Ge$_x$Sn$_{1-x}$O$_2$ epitaxy on TiO$_2$ substrates as well. According to the calculation based on density functional theory, to satisfy the lattice matching condition, x for a and c axis should be $\sim$0.53 and $\sim$0.79, respectively.[2] When it comes to (001) orientation substrates, the in-plane lattice lengths are determined solely by the a axis, thus x should be $\sim$0.53. We first demonstrated near-lattice-matching epitaxy of r-Ge$_{0.66}$Sn$_{0.34}$O$_2$ on an r-TiO$_2$ (001) substrate and observed a significant reduction in dislocations through TEM analysis.[2] Later, Liu et al., reported lattice-matching epitaxy of r-Ge$_{0.54}$Sn$_{0.46}$O$_2$ on r-TiO$_2$ (001) substrate, confirming coherent growth, however, comprehensive structural characterizations were not provided.[33]

In this study, we considered that lattice-matching epitaxy was the preferable method over ELO at the moment, to obtain high-quality alloy films suitable for device applications. We therefore conducted lattice-matching epitaxy of the r-Ge$_x$Sn$_{1-x}$O$_2$ alloy films on r-TiO$_2$ (001) substrates, and thoroughly analyzed the resulting coherent films. Additionally, we successfully demonstrated the device operation of Schottky barrier diodes (SBDs) fabricated on the film.
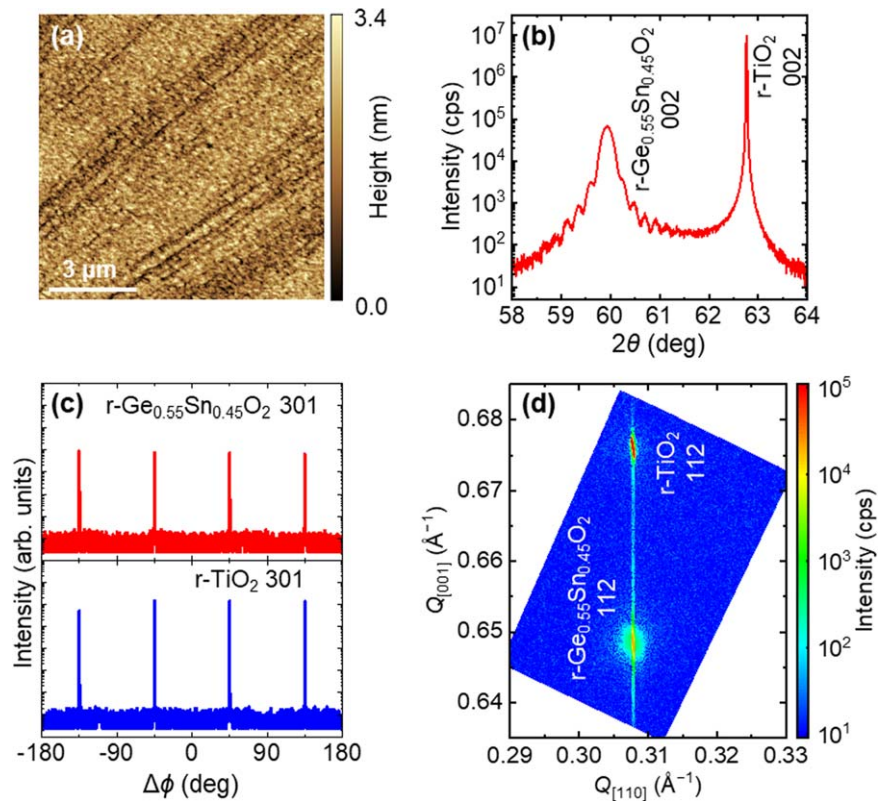
Fig. 1. (a) Surface AFM image of the 48-nm r-Ge$_{0.55}$Sn$_{0.45}$O$_2$ film on r-TiO$_2$ (001) substrate. XRD (b) symmetric θ–2θ scan and (c) skew-symmetric ϕ scan patterns and (d) a RSM of the same sample.

For a series of analyses, five r-Ge$_x$Sn$_{1-x}$O$_2$ films were grown on semi-insulating r-TiO$_2$ (001) substrates (10 × 10 mm^2) by using a hot-wall-type mist CVD method, which is a validated oxide growth method to produce device-quality films.[34] Bis[2-carboxyethylgermanium (IV)] sesquioxide (C$_6$H$_{12}$Ge$_2$O$_7$) and tin (II) chloride dihydrate (SnCl$_2$·2H$_2$O) were used as Ge and Sn precursors, respectively. They were dissolved in pure water with a small amount of hydrochloric acid to prepare a mixed aqueous solution, in which the molar concentrations of Ge and Sn were 0.50 and 0.25 mol l^{-1}, respectively. The precursor solution was atomized by ultrasonic transducers at 2.4 MHz. The generated mist particles were carried into an introduction line and accelerated by O$_2$ gas flows at 3.0 and 0.5 l min^{-1}, respectively, to the surface of the substrate heated at 725 °C in a quartz tube. The grown films were characterized as follows. The x was determined via energy dispersive X-ray spectroscopy (EDS), for which a composition standard was used for calibration. Surface morphology was evaluated utilizing scanning electron microscopy (SEM) with an acceleration voltage of 5 kV and atomic force microscopy (AFM) operating in a contact mode. The epitaxial structure was examined by X-ray diffraction (XRD) measurements using CuK$_{\alpha 1}$ radiation. The thickness was determined by analyzing Laue fringes observed in the θ–2θ scan of the XRD measurement, or a spectrum obtained by ellipsometry. Cross-sectional lattice structures were observed by TEM and scanning TEM (STEM) with an acceleration voltage of 200 kV. Electrical properties, such as carrier density and mobility, were investigated by Hall measurement. To fabricate SBDs, Pt (100 nm) and Ti/Au (75/75 nm) electrodes were deposited onto the film through electron beam evaporation to form anodes and cathodes, respectively. SBDs were characterized using a standard parameter analyzer.

First, we identified the growth mode of the lattice-matched r-Ge$_x$Sn$_{1-x}$O$_2$ films on r-TiO$_2$ substrates by observing the evolution of surface morphology. Four r-Ge$_x$Sn$_{1-x}$O$_2$ films ($x = 0.49$–0.56) were grown for varied times, with the other growth conditions remaining the same. The thicknesses of the grown films were 48, 107, 178, and 478 nm according to the growth times. The composition variation in the films may be attributed to the slight difference in actual growth temperature, which strongly depends on the stability of atomization, because of the high vaporization heat of the mist precursors. Optimizing the operating conditions of the nebulizers for stable mist generation could minimize the composition variation. The SEM observation revealed that the surfaces of all the films were flat and featureless. The AFM observation also confirmed that the RMS roughness of all the films were within the range of 0.2−0.8 nm without thickness dependence. These results imply that the film maintained its surface flatness during the entire growth stages, at least up to 478 nm. This growth behavior can be explained by the Frank–van der Merwe mode, where a 2D heteroepitaxial film grows by complete wetting on the substrate with negligibly small lattice mismatches, and is consistent with our lattice-matching epitaxy. The result differs from the growth behavior of r-SnO$_2$ on r-TiO$_2$, which is dominated by the Volmer–Weber mode,[29,35] where a 3D film grows from the initial stage by strong dewetting on the substrate with large lattice mismatches.

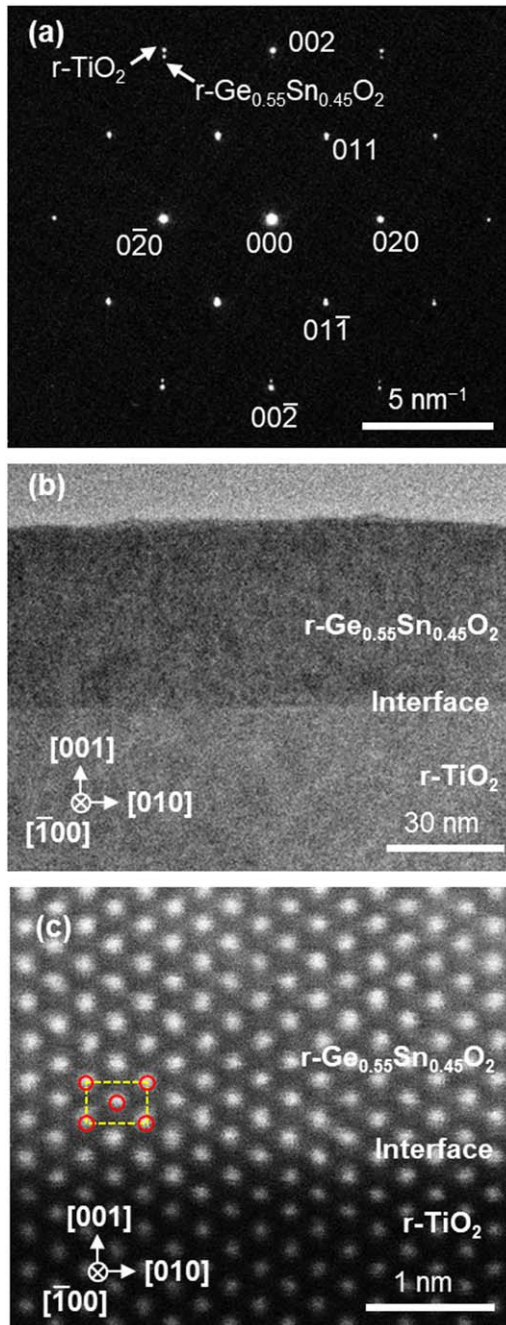The structural properties of the 48 nm-thick lattice-matched film were investigated in detail. Figure 1(a) shows

Fig. 2. (a) SAED pattern, cross-sectional (b) HR-TEM and (c) HAADF-STEM images near the interface of the 48-nm r-$Ge_{0.55}Sn_{0.45}O_2$ film on r-TiO_2 viewed along the [.] zone axis. In (c), the unit cell of the rutile-type structure, where red circles represent metal atoms, is shown to understand Ge and Sn atomic positions.

the AFM image of the surface of the 48-nm r-$Ge_{0.55}Sn_{0.45}O_2$ film on r-TiO_2 (001). The surface morphology was flat with the RMS roughness of 0.66 nm, which is sufficiently smooth for devices that need abrupt interfaces. Figure 1(b) presents the symmetric XRD θ–2θ scan pattern of the same sample. Only the 002 diffraction peaks of the film and substrate appeared. The peak of the film had Laue fringes, indicating its high crystallinity and flatness. It should be noted that no other peaks derived from secondary phase and misoriented domains were detected in the measured 2θ range of 15–95° (not shown). Figure 1(c) shows skew-symmetric XRD ϕ scan patterns of the film and substrate. The 301 diffraction peaks of the film appeared at the same angles as the substrate at 90°

intervals, reflecting a fourfold in-plane rotational symmetry of the (001)-oriented rutile-type structure. Considering these symmetric and skew-symmetric scanning results, the film grew with a tetragonal-on-tetragonal epitaxial relationship to the substrate. In addition, the full width at half maximum values of the ω-rocking curves (ω-FWHMs) of the symmetric 002 and skew-symmetric 301 peaks were 194 and 133 arcsec for the film, and 28 and 35 arcsec for the substrate, respectively. Note that the ω-FWHMs of the 002 and 301 peaks decreased as the film thickness increased (e.g. they were 104 and 90 arcsec, respectively, for the 478-nm film). Figure 1(d) is the XRD reciprocal space map (RSM) taken in the vicinity of the 112 diffraction spots. The spot peak of the film was on the same $Q_{[110]}$ line as the substrate, meaning that they shared the same in-plane lattice constant across a coherent heterointerface as a result of lattice-matching epitaxy.

Next, cross-sectional TEM observations were performed for the same sample to thoroughly examine the microstructure in the vicinity of the heterointerface. Figure 2(a) displays the selected-area electron diffraction (SAED) pattern of the interface. The diffraction spots of the film were close to or overlapped with the substrate spots, reconfirming that the film was single-crystalline without secondary or misoriented domains. Furthermore, the spots of the film had the same in-plane positions as the corresponding substrate spots. This indicates that the lattice of the film was fully constrained to the substrate, which is consistent with the XRD RSM result. Figure 2(b) shows the high-resolution TEM (HR-TEM) image at the interface. The film exhibited uniform image contrast throughout the entire region. The maximum difference in the film thickness was about 4 nm, which agrees with the height scale of the AFM image (3.4 nm) as shown in Fig. 1(a). No threading dislocation was found, even in other observable cross sections of the film in the same specimen (not depicted). This implies that dislocation-free areas of the film were sufficiently large to avoid detection by TEM. Etch pitting of a large surface area of the film may reveal the presence of dislocations, which we will research in the future. Figure 2(c) shows the high-angle annular dark-field STEM (HAADF-STEM) image of the interface. In this image, heavier atoms (Ge/Sn and Ti) were visible as white dots, whereas lighter O atoms were not visible. The arrangement of the Ge/Sn and Ti metal atoms was consistent with that of the rutile-type structure viewed along the same direction (see the schematic unit cell superimposed on the image). At the heterointerface, the darker Ti sublattice transitioned abruptly to the lighter Ge/Sn sublattice with perfect lattice matching. Moreover, the lattice was continuous with no misalignment even to the surface (not shown). The coherent alloy film achieved through lattice-matching epitaxy is expected to have excellent electrical properties, making it highly desirable for use in device applications.

Finally, lateral SBDs were demonstrated using a high-quality r-$Ge_xSn_{1-x}O_2$ alloy film. For this purpose, a 110-nm-thick r-$Ge_{0.49}Sn_{0.51}O_2$ film was prepared on a semi-insulating r-TiO_2 substrate. Although the alloy composition ($x = 0.49$) slightly deviated from the target one ($x = \sim 0.53$), the film still maintained structural coherence, which was confirmed by XRD RSM (not shown). The unintentionally-doped film had good electrical properties with a carrier density (n) of
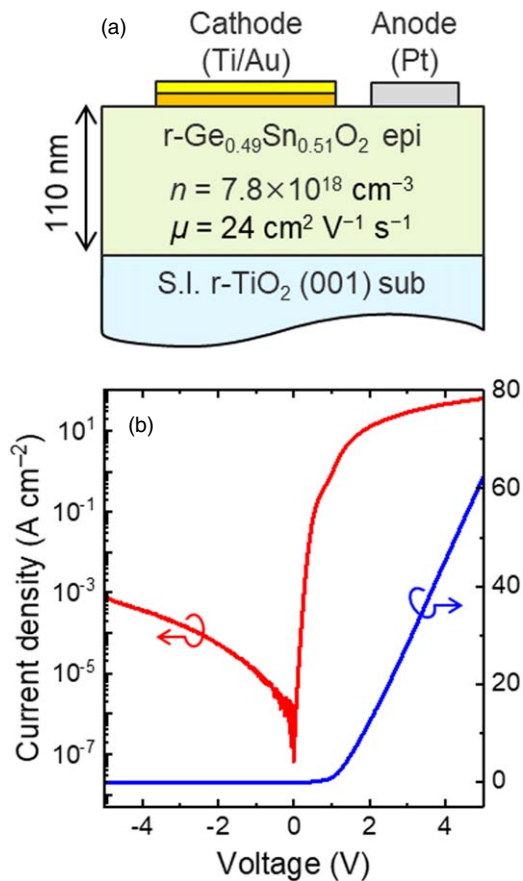
Fig. 3. (a) Schematic of the fabricated SBD. (b) J-V characteristics of the device in semilogarithmic (red) and linear (blue) scales.

$7.8 \times 10^{18} \, \mathrm{cm}^{-3}$ and a mobility (μ) of 24 cm^2 V^{-1} s^{-1}, respectively. By forming Ti/Au cathodes and Pt anodes on the front surface, lateral SBDs were fabricated as illustrated in Fig. 3(a). The Ti/Au cathodes acted properly as ohmic contacts, as confirmed by current density (J)-voltage (V) curves with linear dependencies (not shown). Meanwhile, the J-V curve of the SBD displayed a clear rectifying property with a rectification ratio of 8.2×10^4 at ± 5 V, as shown in Fig. 3(b), indicating that the Pt anode behaved as a Schottky contact. In addition, the on-resistance was as high as 60 mΩ cm^2 and the breakdown voltage, at which J reached 10^{-4} A cm^{-2}, was as low as -2.5 V. These poor device characteristics are probably attributed to the lateral device configuration and high n. They need to be improved by using doping-controlled films with lower n on conductive Nb-doped TiO$_2$ substrates, which is our future work.

In conclusion, our study sought to explore the potential of the r-Ge$_x$Sn$_{1-x}$O$_2$ alloy semiconductor. To achieve this, we utilized the lattice-matching strategy to attain single-crystal-line coherent films with flat surfaces and no TEM-detectable dislocations on isostructural r-TiO$_2$ substrates. The quality of the films is high enough to fabricate SBDs with high rectification ratios. We anticipate that this first device demonstration encourages more researchers to enter the field of r-Ge$_x$Sn$_{1-x}$O$_2$ alloy.

ORCID iDs   Hitoshi Takane https://orcid.org/0000-0001-8866-145X
Takayoshi Oshima https://orcid.org/0000-0001-8550-9735
Takayuki Harada https://orcid.org/0000-0002-8657-2258
Kentaro Kaneko https://orcid.org/0000-0001-6626-7611
Katsuhisa Tanaka https://orcid.org/0000-0002-1409-2802

1) S. Chae et al., Appl. Phys. Lett. **118**, 260501 (2021).
2) H. Takane, Y. Ota, T. Wakamatsu, T. Araki, K. Tanaka, and K. Kaneko, Phys. Rev. Mater. **6**, 084604 (2022).
3) M. Stapelbroek and B. D. Evans, Solid State Commun. **25**, 959 (1978).
4) S. Chae, J. Lee, K. A. Mengle, J. T. Heron, and E. Kioupakis, Appl. Phys. Lett. **114**, 102104 (2019).
5) C. A. Niedermeier, K. Ide, T. Katase, H. Hosono, and T. Kamiya, J. Phys. Chem. C **124**, 25721 (2020).
6) K. A. Mengle, S. Chae, and E. Kioupakis, J. Appl. Phys. **126**, 085703 (2019).
7) K. Bushick, K. A. Mengle, S. Chae, and E. Kioupakis, Appl. Phys. Lett. **117**, 182104 (2020).
8) S. Chae, H. Paik, N. M. Vu, E. Kioupakis, and J. T. Heron, Appl. Phys. Lett. **117**, 072105 (2020).
9) H. Takane and K. Kaneko, Appl. Phys. Lett. **119**, 062104 (2021).
10) W. Chen, K. Egbo, H. Tornatzky, M. Ramsteiner, M. R. Wagner, and O. Bierwagen, APL Mater. **11**, 071110 (2023).
11) T. Minami, Semicond. Sci. Technol. **20**, S35 (2005).
12) Y. Furubayashi, T. Hitosugi, Y. Yamamoto, K. Inaba, G. Kinoda, Y. Hirose, T. Shimada, and T. Hasegawa, Appl. Phys. Lett. **86**, 252101 (2005).
13) R. E. Presley, C. L. Munsee, C. H. Park, D. Hong, J. F. Wager, and D. A. Keszler, J. Phys. D: Appl. Phys. **37**, 2810 (2004).
14) M. Katayama, S. Ikesaka, J. Kuwano, Y. Yamamoto, H. Koinuma, and Y. Matsumoto, Appl. Phys. Lett. **89**, 242103 (2006).
15) K. Reimann and M. Steube, Solid State Commun. **105**, 649 (1998).
16) J. Pascual, J. Camassel, and H. Mathieu, Phys. Rev. B **18**, 5606 (1978).
17) M. Nagasawa, S. Shionoya, and S. Makishima, Jpn. J. Appl. Phys. **4**, 195 (1965).
18) H. F. Kunkle and E. E. Kohnke, J. Appl. Phys. **36**, 1489 (1965).
19) V. Agafonov, D. Michel, M. Perez y Jorba, and M. Fedoroff, Mater. Res. Bull. **19**, 233 (1984).
20) Z. Galazka et al., Phys. Status Solidi A **211**, 66 (2014).
21) S. Chae et al., J. Vac. Sci. Technol. A **40**, 050401 (2022).
22) Y. Nagashima, M. Fukumoto, M. Tsuchii, Y. Sugisawa, D. Sekiba, T. Hasegawa, and Y. Hirose, Chem. Mater. **34**, 10842 (2022).
23) H. Takane, I. Kakeya, H. Izumi, T. Wakamatsu, Y. Isobe, K. Kaneko, and K. Tanaka, J. Appl. Phys. **134**, 165706 (2023).
24) H. Wakabayashi, T. Suzuki, Y. Iwazaki, and M. Fujimoto, Jpn. J. Appl. Phys. **40**, 6081 (2001).
25) M. Fukumoto, S. Nakao, K. Shigematsu, D. Ogawa, K. Morikawa, Y. Hirose, and T. Hasegawa, Sci. Rep. **10**, 6844 (2020).
26) T. Z. Win, K. Inaba, S. Kobayashi, Y. Kanetake, and Y. Nakamura, Trans. Mater. Res. Soc. Jpn. **45**, 173 (2020).
27) A. Usui, H. Sunakawa, A. Sakai, and A. A. Yamaguchi, Jpn. J. Appl. Phys. **36**, L899 (1997).
28) O.-H. Nam, M. D. Bremser, T. S. Zhelava, and R. F. Davis, Appl. Phys. Lett. **71**, 2638 (1997).
29) H. Takane, T. Oshima, K. Tanaka, and K. Kaneko, Appl. Phys. Express **16**, 045503 (2023).
30) M. Kondow, K. Uomi, A. Niwa, T. Kitatani, S. Watahiki, and Y. Yazawa, Jpn. J. Appl. Phys. **35**, 1273 (1996).
31) R. Butté et al., J. Phys. D: Appl. Phys. **40**, 6328 (2007).
32) W. H. Baur and A. A. Khan, Acta Crystallogr. Sect. B **27**, 2133 (1971).
33) F. Liu, T. K. Truttmann, D. Lee, B. E. Matthews, I. Laraib, A. Janotti, S. R. Spurgeon, S. A. Chambers, and B. Jalan, Commun. Mater. **3**, 69 (2022).
34) H. Takane, Y. Ando, H. Takahashi, R. Makisako, H. Ikeda, T. Ueda, J. Suda, K. Tanaka, S. Fujita, and H. Sugaya, Appl. Phys. Express **16**, 081004 (2023).
35) M. Y. Tsai, M. E. White, and J. S. Speck, J. Cryst. Growth **310**, 4256 (2008).